Korean J. Chem. Eng., 32(8), 1578-1585 (2015)
DOI: 10.1007/s11814-014-0379-6

pISSN: 0256-1115
eISSN: 1975-7220

Photocatalytic degradation of 2,4-dichlorophenol over Fe-ZnO catalyst under visible light

Pradabduang Kiattisaksiri*,, Pummarin Khamdahsag***, Pongtanawat Khemthong***, Nuttaporn Pimpha***, and Nurak Grisdanurak****,†**

*International Program in Hazardous Substance and Environmental Management, Graduate School, Chulalongkorn University, Bangkok 10330, Thailand
**Center of Excellence on Hazardous Substance Management (HSM), Bangkok 10330, Thailand
***National Nanotechnology Center, Thailand Science Park, Pathumthani 12120, Thailand
****Department of Chemical Engineering, Faculty of Engineering, Thammasat University, Pathumthani 12121, Thailand
(*Received 16 June 2014 • accepted 20 December 2014*)

Abstract—Fe-ZnO was synthesized via impregnation and applied to photocatalytic degradation of 2,4-dichlorophenol (2,4-DCP) under visible light. Conditions of Fe-ZnO synthesis which included a Fe content and a calcination temperature were focused. From UV-DRS, visible light absorption of Fe-ZnO samples increased with increasing of Fe content and calcination temperature. TEM images revealed Fe species (FeO, Fe_3O_4, and Fe_2O_3) on ZnO as a function of calcination temperature. XANES analysis confirmed the majority of Fe^{3+} content. Response surface methodology (RSM) dominating over experimental design and statistical analysis for 2,4-DCP photocatalytic degradation indicated that the high degradation efficiency was associated with calcination temperature of 680-700 °C, Fe content of 4.5-5.0 mol%, and catalyst loading of 1.2-1.8 g L^{-1}. Moreover, addition of 2 mM of $K_2S_2O_8$ in a 5.0Fe-ZnO@700 °C system could enhance the degradation efficiency to a completion within 90 min. The kinetics of 2,4-DCP photocatalytic degradation well fit the Langmuir-Hinshelwood model.

Keywords: Fe-ZnO, Impregnation, Photocatalysis, Visible Light, Response Surface Methodology

INTRODUCTION

2,4-Dichlorophenol (2,4-DCP) is potentially carcinogenic and disturbs human and animal endocrine systems [1]. It has been introduced into the environment as a result of several man-made activities such as uncontrolled uses of pesticides and herbicides and wastewater effluent. Due to its toxicity and persistence in the environment, 2,4-DCP is listed in priority control pollutants by the US EPA Clean Water Act [2].

Various methods have been offered to degrade 2,4-DCP contaminant, like biodegradation and adsorption [3], but this compound is highly resistant to bio-treatment, and the need of activated carbon regeneration renders this process both inconvenient and costly. Heterogeneous photocatalysis as an advanced oxidation process (AOPs) has been extensively developed. This method provides high degradation efficiency by the generation of hydroxyl radicals ($OH^{\bullet}$), and the oxidizing radical allows the strong destruction of organic pollutants with non-selectivity.

Heterogeneous photocatalysis is based on metal oxide material, which is classified as a semiconductor, activated by the absorption of the light. While TiO_2 have been used as an effective catalyst, numerous studies have evaluated the potential of other catalysts. Among others, ZnO appears to be a suitable alternative to TiO_2 and was reported to be more efficient than TiO_2 in some photoreactions of phenolic compounds [4]. However, the most restricting factor for ZnO is its wide band gap energy (E_g) about 3.2 eV [5], which only requires energy of UV light. Unfortunately, the solar spectrum consists only 3-4% of UV light, while 46% and 47% of the spectrum are visible light and infrared radiation, respectively. To extend the photocatalytic properties into the visible light region, various metal and non-metal ions have been doped into catalysts [6-8]. Among various dopants, Fe was proved to be a successful doping element. A modification of catalyst by doping Fe provided the red shift in the UV-Vis spectra due to the introduction of the 3d electron state of Fe^{3+}, $3d^5$, in the conduction band of the catalyst [7]. Moreover, Fe-doped catalyst showed a stronger absorption in the visible region, compared to the non-doped catalyst and also exhibited good photoactivity for the degradation of organic pollutant in wastewater under visible light irradiation [9].

Accordingly, we focused on a modification of ZnO by Fe doping (Fe-ZnO) to increase its application in visible light region and examined its photocatalytic characteristics by the degradation of aqueous 2,4-DCP.

EXPERIMENTAL

1. Experimental Design and Statistical Analysis

Response surface methodology (RSM) is an empirical model used to evaluate the relationship between a set of controllable experimental factors and observed results [10]. RSM analysis is able to

†To whom correspondence should be addressed.
E-mail: gnurak@engr.tu.ac.th

Table 1. Ranges and levels of independent parameters

No.	Parameter	Unit	Range and level of actual value	
			−1	+1
1	Fe content	mol%	0.5	5.0
2	Calcination temperature	°C	400	700
3	Catalyst loading	g L^{-1}	0.50	2.00

determine whether a factor is significant by referring to the '*p*-value' based on the analysis results. To determine whether the factor is affecting the degradation percentage of 2,4-DCP, the '*p*-value' should be less than 0.5.

In this study, RSM experiments based on 3-level factorial were adopted with a quadratic model to find the optimal operating conditions for the further step of laboratory work. The experimental data was analyzed statistically using Minitab® 15 software (Minitab Inc.). Based on three central points and two replicates, the total number of experiment in this study was 30. Three parameters of Fe content, calcination temperature, and catalyst loading were studied. The experiment was performed in a random manner to avoid any systematic bias for the outcomes.

2. Fe-ZnO Catalyst Preparation

$Fe(NO_3)_3{\cdot}9H_2O$ (99%, Merck) corresponding to 0.5, 2.5, and 5.0 mol% of Fe in commercial ZnO nanopowder (>99.7%, Inframat® Advanced Materials) was dissolved in deionized water. The solution was added via dropping onto ZnO nanopowder. The obtained material was sonicated for 30 min. After the impregnation process, it was dried at 70 °C for 36 hr and ground. Finally, the catalyst was calcined under air at 400, 550, and 700 °C with heating rate of 2 °C min^{-1} for 3 hr.

Crystalline structure and phase of Fe-ZnO samples were characterized by X-ray diffractometer (XRD, Bruker-8). XRD spectrum was determined using Cu Kα radiation at a wavelength of 0.15406 nm, scanned in the 2θ range from 20-80°, and operated at 40 kV and 40 mA. Specific surface area was obtained by nitrogen adsorption at −196 °C on a Quantachrome instruments (AUTOSORB-1) sorption. Prior to the measurement, sample was degassed at 250 °C for 2 hr. The specific surface area was calculated using Brunauer-Emmett-Teller (BET) method. Scanning electron microscopy (SEM, JSM-6400, 20kX) and transmission electron microscopy (TEM, JEM-2100, 200kV) were used for inspecting morphology of the sample. Absorption property was investigated on UV-Vis diffuse reflectance spectroscopy (UV-DRS, Hitachi U-3501), using $BaSO_4$ as a reflectance standard. X-ray absorption near edge structure (XANES) measurement was performed at Beamline 8: XAS, Synchrotron Light Research Institute, Thailand. A double Ge(220) crystal monochromator was employed for selection of photon energy. The data was obtained at room temperature in fluorescence mode. The XANES spectra were analyzed using Athena program. In addition, zeta potential was measured by a zeta meter (Zeta meter system 3.0+).

3. Photocatalytic Degradation of 2,4-DCP

A batch photoreactor of 250 mL was configured with a 1,500 W Xenon lamp (visible light intensity 500 Wm^{-2}). Light array was cut off at 400 nm by 1 M of sodium nitrite ($NaNO_2$). A magnetic stirrer was located at the photoreactor's base to ensure homogeneous mixing of the solution throughout the reaction. A reaction temperature was controlled at 25 °C. 2,4-DCP solution was prepared by deionized water. After that, Fe-ZnO catalyst was dispersed into the solution. The initial pH of the solution was adjusted to pH 8.5 with HNO_3 and NaOH. The suspension was stirred in the dark for 60 min, and then 2 mM $K_2S_2O_8$ was added. After that, the lamp was switched on to initiate the reaction. 1.5 mL of the sample was withdrawn from the reactor at different reaction times. A blank test was also performed by irradiating 2,4-DCP solution without the presence of catalyst under visible light irradiation for checking the photolysis. The concentration of 2,4-DCP in the filtrate was measured by high performance liquid chromatography with diode-array detector (HPLC-DAD 1200 series detector, 1100 series pump and controller, Agilent technologies).

RESULTS AND DISCUSSION

1. Characterization

XRD patterns of Fe-ZnO samples compared with bare ZnO nanopowder and Fe_2O_3 are shown in Fig. 1. All samples exhibited the characteristic peaks of hexagonal wurtzite ZnO at (100), (002), (101), (102), (110), (103), and (112) planes, which corresponded to the standard JCPDS file no.36-1451 [11]. However, the content of Fe might be too small to determine its existence, which possibly indicated that Fe was well dispersed onto the surface of ZnO nanopowder.

The diffraction peaks at 2θ around 29.5° were observed in bare ZnO nanopowder, and the 5.0Fe-ZnO samples calcined at 400 and 550 °C. It might be indicated to (111) plane of ZnS which corresponded to cubic zinc blend structure [12-14], or (002) plane of Zn_xSr_xS in rocksalt structure [15], which was possibly contaminated during the production of ZnO nanopowder. This peak also gradually decreased with increasing calcination temperature. The possible reason is that high temperature could accelerate the oxidation of sulfur to obtain ZnO. It can be inferred that both cubic zinc blend

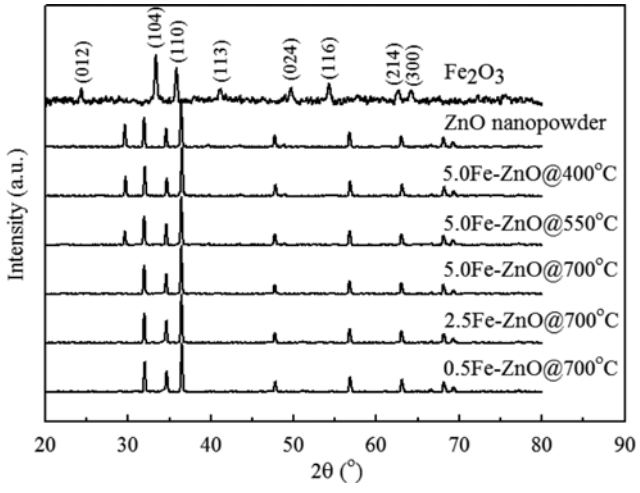

Fig. 1. Normalized XRD patterns of Fe-ZnO samples at different Fe contents calcined at 700 °C and 5.0Fe-ZnO samples at different calcination temperatures.

Table 2. Crystalline sizes and specific surface areas of ZnO nanopowder and Fe-ZnO samples

Sample	Crystal size (nm)	Specific surface area ($m^2 g^{-1}$)
ZnO nanopowder	35.93	4.48
0.5Fe-ZnO@700 °C	37.58	4.90
2.5Fe-ZnO@700 °C	37.58	4.98
5.0Fe-ZnO@700 °C	37.74	5.52
5.0Fe-ZnO@550 °C	37.74	7.39
5.0Fe-ZnO@400 °C	35.95	7.75

structure and rocksalt structure had been transformed into wurtzite phase of ZnO.

Crystalline size of wurtzite ZnO at (101) plane is given in Table 2. When Fe content increased for Fe-ZnO samples calcined at 700 °C, the crystalline size was slightly increased. In addition, crystalline size was found enlarged for 5.0Fe-ZnO samples after raising the calcination temperature. However, they were not significantly different. Table 2 also presents the specific surface area of Fe-ZnO, which increased with increasing of Fe content, but decreased with increasing of calcination temperature. The increment of crystalline size and specific surface area at higher calcination temperature was probably caused by the particle aggregation and sintering.

Surface morphology of the samples observed from SEM images is shown in Fig. 2. ZnO nanopowder was revealed in rectangular chunk shape, but Fe-ZnO samples were slightly different with small spheres on the rectangular chunk [16]. Effect of Fe content in samples calcined at 700 °C could not be differentiated clearly by SEM. However, the change of the small spheres for 5.0Fe-ZnO samples calcined at different temperature was noticed and corresponded to the specific surface area stated in Table 2.

Fig. 3 shows the UV-DRS spectra of Fe-ZnO prepared at different Fe contents and 5.0Fe-ZnO calcined at different temperatures. It can be seen that the spectrum of ZnO nanopowder hardly presented absorption band in the visible region (440-700 nm) related to other reports [17,18]. A significant increase in the absorption at

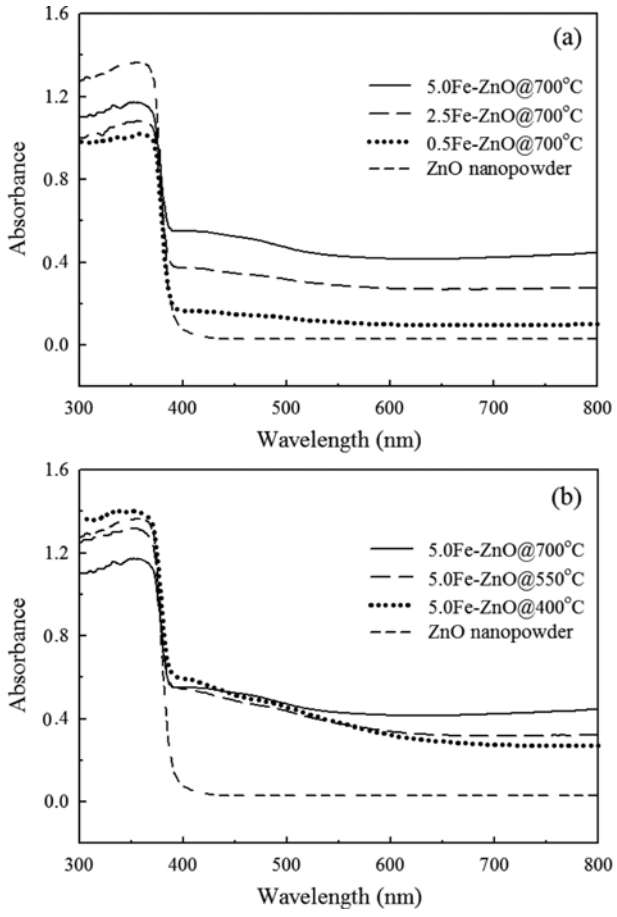

Fig. 3. UV-DRS spectra of (a) Fe-ZnO samples at different Fe contents calcined at 700 °C and (b) 5.0Fe-ZnO samples at different calcination temperatures.

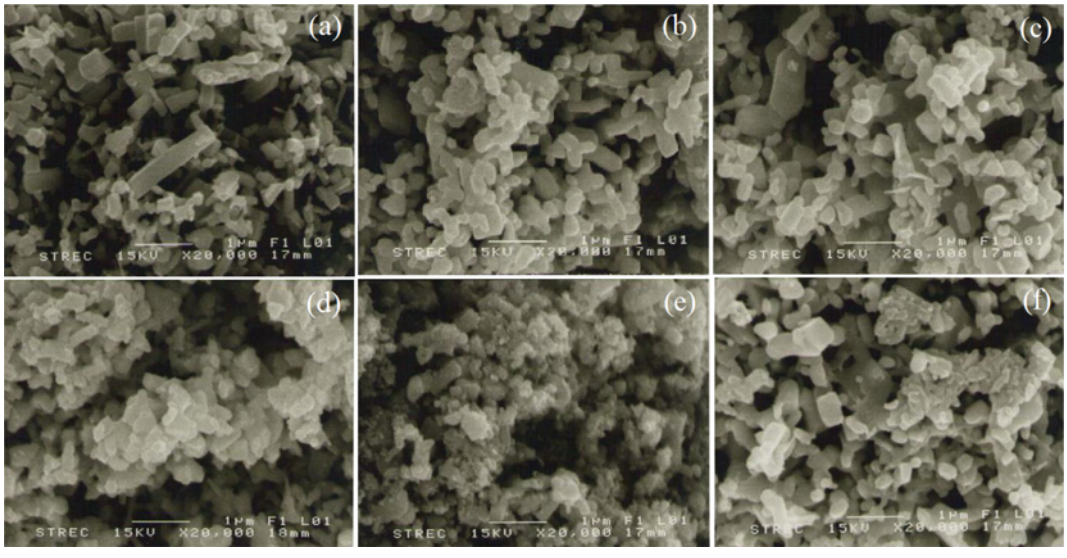

Fig. 2. SEM images of (a) ZnO nanopowder, (b) 0.5Fe-ZnO@700 °C, (c) 2.5Fe-ZnO@700 °C, (d) 5.0Fe-ZnO@400 °C, (e) 5.0Fe-ZnO@550 °C, and (f) 5.0Fe-ZnO@700 °C.

wavelengths shorter than 400 nm could be assigned to the intrinsic band gap absorption of ZnO (3.2 eV). Fig. 3(a) reveals that the samples with higher Fe content displayed stronger absorption band in the visible range [17,19]. Fig. 3(b) also discloses the superior adsorption band at the last region of visible wavelength (550-700 nm) of 5.0Fe-ZnO calcined at higher temperature [18]. The absorption increased with increasing the Fe content and calcination temperature accompanied by changing the color of the samples from cream to grey-brown. In addition, the formation of Fe dopant energy level below conduction band of ZnO might have taken place through calcination treatment. The band gap energy (E_g) for all samples was determined by fitting the absorption data to the transition equation. According to the Tauc plots between $(ah\nu)^{1/2}$ versus photon energy ($h\nu$) from the Kubelka-Munk function [20-22], the E_g of Fe-ZnO samples as well as that of ZnO nanopowder was about 3.11 eV, which was close to the value of ZnO in another report [23]. The unchanged E_g indicated that most Fe ions had not incorporated in ZnO [18]. In summary, both Fe content and calcination temperature had no effect on the E_g shift of the samples but on visible region absorption, contributing the possibility for visible-light-driven photocatalytic degradation of 2,4-DCP.

The TEM images of ZnO nanopowder and 5.0Fe-ZnO as function of temperature are in Fig. 4. The particles of ZnO nanopowder were mostly rectangular, in Fig. 4(a), whereas 5.0Fe-ZnO tended to appear more spherical, in Figs. 4(b) and 4(c), as found in SEM results. The agglomeration was clearly observed with the highest calcination temperature, in Fig. 4(d). Calcination temperature showed a significant effect on the morphology of 5.0Fe-ZnO catalyst. From the high resolution TEM image for 5.0Fe-ZnO calcined at 400 °C

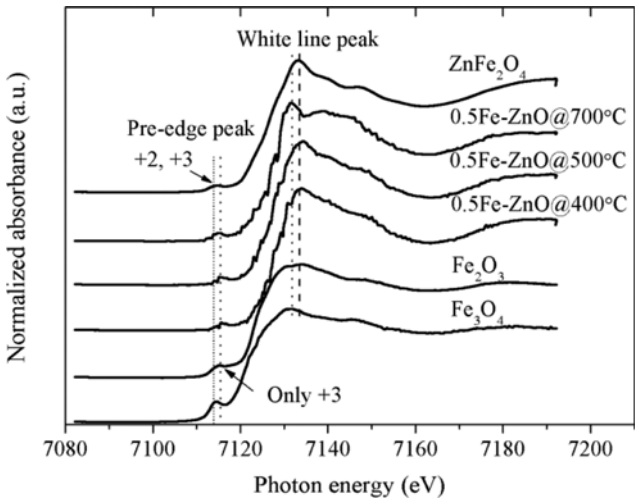

Fig. 5. Fe K-edge XANES spectra of 5.0Fe-ZnO samples at different calcination temperatures.

in Fig. 4(e), the lattice *d*-spacing of 0.24 nm corresponding to (111) plane of FeO [24] was indicated as well as that of 0.48 and 0.29 nm, complying with (111) and (220) planes of Fe_3O_4 [25]. Besides, those two planes of Fe_3O_4 were discovered in 5.0Fe-ZnO calcined at 550 °C in Fig. 4(f) together with appearance of α-Fe_2O_3. For 5.0Fe-ZnO calcined at 700 °C in Fig. 4(g), the lattice *d*-spacing of 0.27 nm according with (104) plane of α-Fe_2O_3 was only identified [26]. This evidence conformed to phase transformation of Fe via calcination under atmospheric pressure, which started by occurrence of FeO→

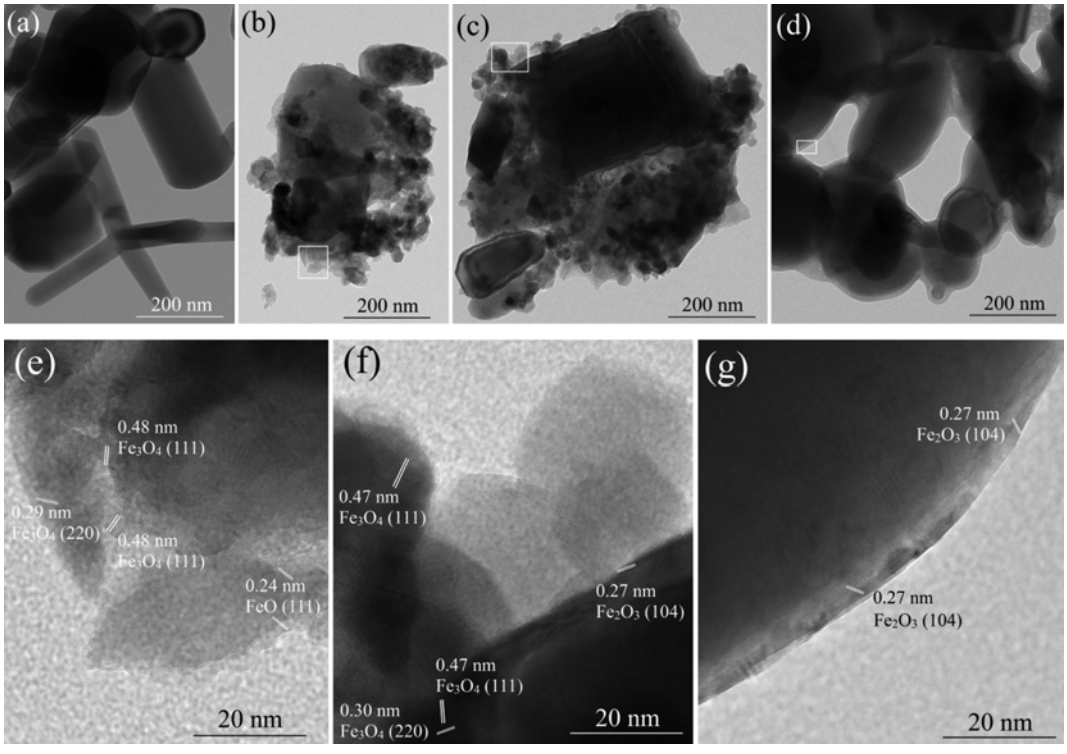

Fig. 4. TEM images of (a) ZnO nanopowder, (b) 5.0Fe-ZnO@400 °C with inset (e), (c) 5.0Fe-ZnO@550 °C with inset (f), and (d) 5.0Fe-ZnO@700 °C with inset (g).

$Fe_3O_4 \rightarrow \alpha$-$Fe_2O_3$ [27]. The transformation to Fe_2O_3 which originated at calcination temperature higher than 500 °C [28] agreed with our result from TEM images.

According to the XANES results, the relationship of the Fe^{2+} and Fe^{3+} is displayed in Fig. 5. All the Fe oxide samples showed a pre-edge energy approximately at 7,113 eV. The pre-edge peak also shifted to a higher energy with an increase in the valence state of the absorber atom. We observed that both the pre-edge and white line peaks of 0.5Fe-ZnO samples are between those of Fe^{3+} and Fe^{2+} and closer to Fe^{3+}, which indicated that there was a mix of 2+ and 3+ valence states, and Fe^{3+} was in the majority. This result was well consistent with the TEM images of samples presented previously. A dominant pre-edge peak in XANES spectrum of 0.5Fe-ZnO could be attributed to the 1s→3d electronic transition in centrosymmetric structure of iron, which confirmed that the major iron cation in the ZnO matrix was Fe^{3+} oxidation state. Moreover, the differences between the XANES spectra of 0.5Fe-ZnO samples calcined at 400, 500, and 700 °C could be identified by their pre-edge and white line peaks. The white line curve of 0.5Fe-ZnO calcined at 700 °C shows two main peaks attributed to the features of Fe_3O_4 and Fe_2O_3. Moreover, some of the Fe^{3+} in 0.5Fe-ZnO calcined at 700 °C successfully substituted for the lattice site of Zn^{2+} and generates single-phase $Zn_{1-x}Fe_xO$ [29].

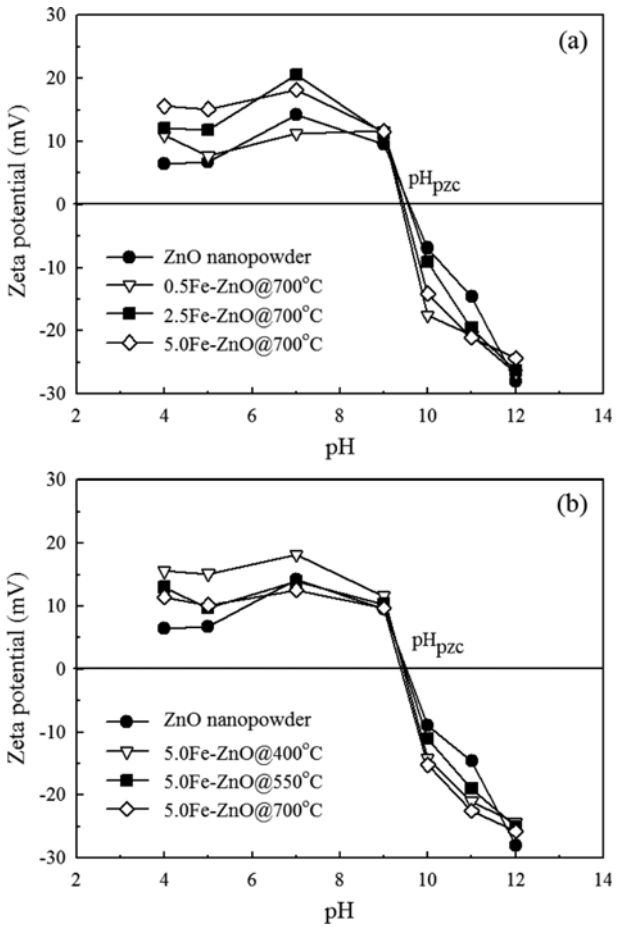

Fig. 6. Zeta potential plots as a function of pH of (a) Fe-ZnO samples at different Fe contents calcined at 700 °C and (b) 5.0Fe-ZnO samples calcined at 400-700 °C.

Fig. 6 shows the zeta potential of all catalysts with respect to solution pH. The point of zero charge (pH_{pzc}) of bare ZnO nanopowder and Fe-ZnO samples was found at pH 9.5. The pH_{pzc} of the samples had no shift according to both Fe content and calcination temperature effects. The surface of catalyst therefore presented a positive charge with pH<9.5. Considering a pK_a of 2,4-DCP, its value is 7.89 [30], meaning that the pollutant exists mainly in anionic form with pH of the solution higher than its pK_a. It could be inferred that more 2,4-DCP would be adsorbed on catalysts surface at pH between the pKa of 2,4-DCP (7.89) and the pH_{pzc} (9.5) of the catalysts due to the opposite charge. Therefore, solution pH was fixed at 8.5.

2. Photocatalytic Testing of 2,4-DCP

2-1. Experimental Design Analysis

Three-level factorial was used to evaluate 2,4-DCP photocatalytic degradation. Parameters of Fe content, calcination temperature, and catalyst loading were involved as degradation key parameters while some factors such as initial concentration of 2,4-DCP (5 mg L^{-1}), pH (8.5), and $K_2S_2O_8$ concentration (2 mM) were fixed. The percent degradation was considered as a response variable.

2-2. Model Validation

Significant factors for the degradation were evaluated based on 95% confidence interval and *p*-values less than 0.05. A degradation model based quadratic pattern was established, shown in Eq. (1). All individual factors were significant, while interactive factors of Fe content-calcination temperature, Fe content-catalyst loading, and calcination temperature-catalyst loading were significant.

$$\begin{aligned}\%\ \text{Degradation} = {} & 135.97 - 14.809\ \text{Fe content} \\ & - 0.459\ \text{calcination temperature} \\ & + 28.094\ \text{loading} \\ & + 0.026\ \text{Fe content-calcination temperature} \\ & - 0.616\ \text{Fe content-catalyst loading} \\ & + 0.018\ \text{calcination temperature-catalyst loading} \\ & + 0.559\ \text{Fe content}^2 + (3.667\times10^{-4}) \\ & \times \text{calcination temperature}^2 - 11.571\ \text{catalyst loading}^2 \quad (1)\end{aligned}$$

A parity plot of actual and predicted results is shown in Fig. 7. A

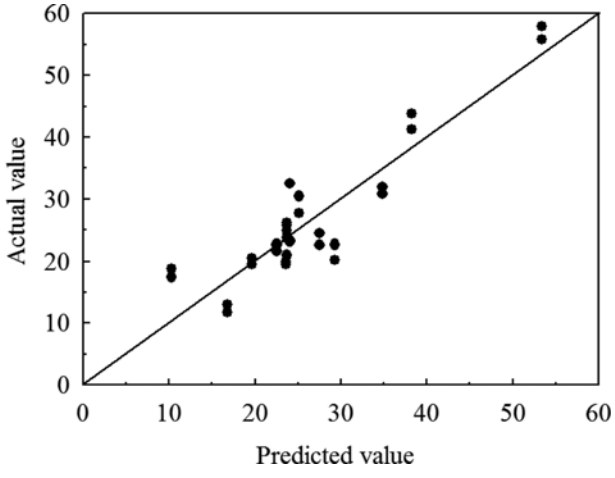

Fig. 7. A parity plot of percent degradation.

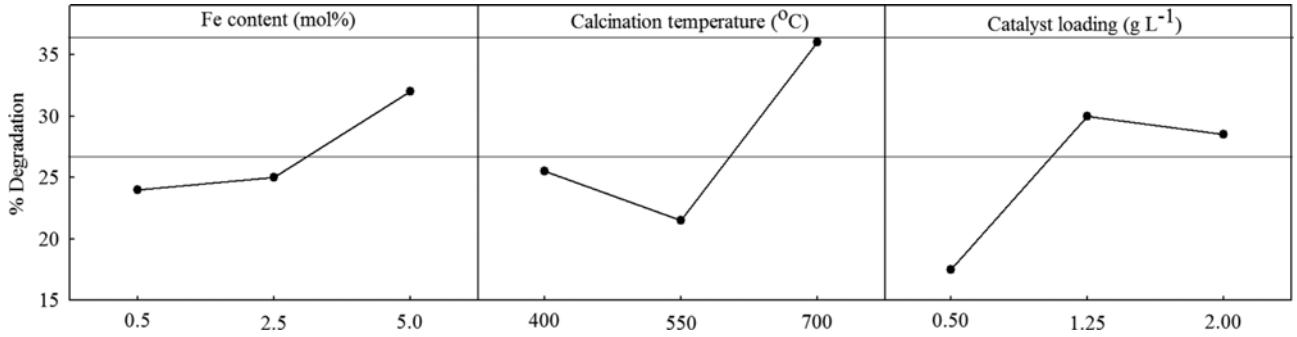

Fig. 8. Main effect plots for percent degradation of 2,4-DCP.

correlation factor was approximately equal to 0.824. ANOVA was used to check the significance and adequacy of the model. Fischer's F test (*F*-value) is a statistically valid measure of how well the factors describe the variation in the data about its mean [31]. It is the ratio of sum square regression to sum square residual error. A value greater than 4.0 is generally desirable. In this work, the ratio of sum square regression to sum square residual error turned to be 4.819 (2795.44/580.11). It was greater than 4.0, indicating that the model was adequate significantly for 2,4-DCP photocatalytic degradation.

2-3. Main Effect Investigation

Fig. 8 shows degradation plots of 2,4-DCP on different main factors. As related to other studies [17,32], the more Fe doped onto ZnO, the higher percent degradation was observed corresponding to higher light absorption in visible range as shown in UV-DRS spectra.

Mild calcination temperatures (400 and 550 °C) did not affect the catalytic activity, while the degradation efficiency was increased by calcination at 700 °C. This result agreed with the XRD pattern, which showed that some metal or unstable phase could be taken out from ZnO at 700 °C.

The removal efficiency tended to be increased with increasing the catalyst loading from 0.5 to 1.25 g L^{-1}. However, the degradation efficiency slightly decreased when 2.0 g L^{-1} of the catalyst loading was used. This was probably because excess catalyst particles led to the excessive opacity and screening effect; therefore, the light penetration was hindered [33].

The study of the response surfaces and contour graphs provides a simple method to optimize the efficiency of the treatment and contributes to the identification of the interactions between the variables. The surface and contour plots are given in Fig. 9. The effect of calcination temperature and Fe content is shown in Fig. 9(a). The high degradation efficiency was associated with high calcination temperature (680-700 °C), and evaluated Fe content (4.5-5.0 mol%). Strong evidence of interaction between catalyst loading and Fe content is shown in Fig. 9(b). Similarly, the largest percent degradation was observed for high Fe content (4.5-5.0 mol%) as the catalyst loading in the level of 1.2-1.8 g L^{-1}. The data presented in Fig. 9(c) describes the impact of catalyst loading and calcination temperature. The plot shows that the level of the catalyst loading in range of 1.2-2.0 g L^{-1} was more highly effective with calcination at high temperature (680-700 °C).

From the 3-level factorial analysis, the optimal operating parameter which was selected to apply further in the next our experiment was of Fe content of 5.0 mol%, calcination temperature of 700 °C, and catalyst loading of 1.5 g L^{-1}.

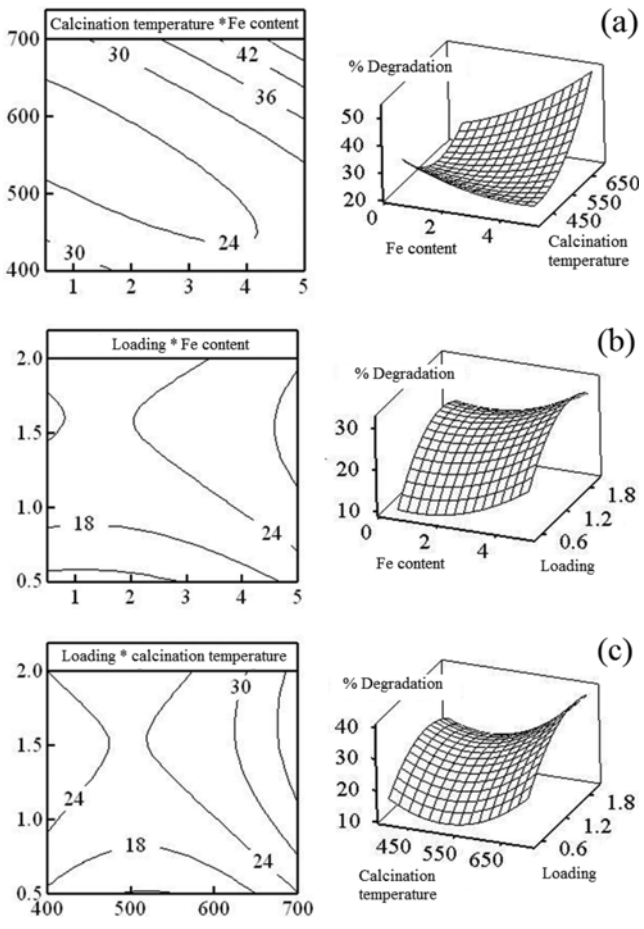

Fig. 9. Contour and surface plots on effects of (a) calcination temperature (°C) and Fe content (mol%), (b) catalyst loading (g L^{-1}) and Fe content (mol%), and (c) catalyst loading (g L^{-1}) and calcination temperature (°C).

3. Kinetic Study

The optimal conditions (1.5 g L^{-1} of 5.0Fe-ZnO@700 °C) obtained from the 3-level factorial analysis were selected to study the kinetics of 2,4-DCP photodegradation. The study lasted 120 min, shown in Fig. 10(a). A control experiment under visible light illustrated that the degradation of 2,4-DCP was less than 4.0% under the direct photolysis. $K_2S_2O_8$ alone was not effective much for 2,4-DCP deg-

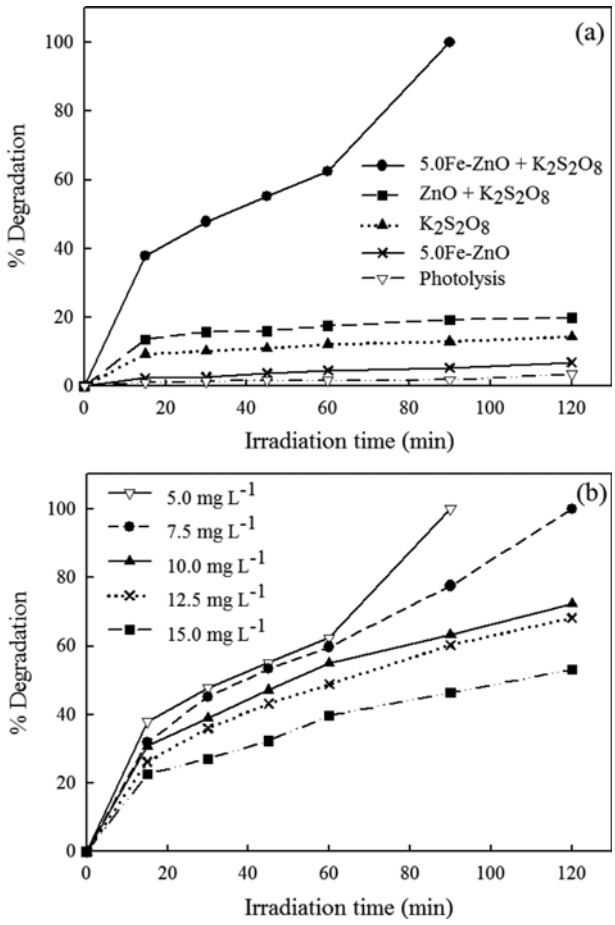

Fig. 10. Percent degradation of 2,4-DCP under (a) various catalytic conditions at 5.0 mg L^{-1} of 2,4-DCP, (b) effect of 2,4-DCP initial concentration using 5.0Fe-ZnO@700 °C (controlled parameters: 1.5 g L^{-1} of catalyst loading, and pH 8.5).

radation (less than 14.0% in 120 min). However, the degradation efficiency reached 100% within 90 min with a combination of 5.0Fe-ZnO@700 °C and $K_2S_2O_8$. This probably could be explained via the following reactions:

$$S_2O_8^{2-} + e^-_{CB\,(ZnO)} + h\nu \rightarrow SO_4^{2-} + SO_4^{\bullet-} \quad (2)$$

$$SO_4^{\bullet-} + H_2O + h\nu \rightarrow SO_4^{2-} + OH^{\bullet} + H^+ \quad (3)$$

$$SO_4^{\bullet-} + 2,4\text{-DCP} + h\nu \rightarrow SO_4^{2-} + \text{Oxidized species} \quad (4)$$

The presence of $S_2O_8^{2-}$ was sufficient to oxidize 2,4-DCP in the presence of catalyst under visible light irradiation. This is because $S_2O_8^{2-}$ can generate the sulfate radical anions (SO_4^{2-}), which are very strong oxidizing species. Additionally, $SO_4^{\bullet-}$ increases the degradation efficiency by minimizing e^--h^+ recombination.

According to TEM and XANES results, which indicated the domination of Fe^{3+} over other Fe species especially for 5.0Fe-ZnO@700 °C, the 2,4-DCP photocatalytic degradation efficiency was enhanced by ZnO doped by Fe^{3+}. Additionally, the positively charge metal ions on ZnO surface was easily reduced by e^- in conduction band, and thus increased the charge separation as given by following reactions [34]:

$$Fe^{3+} + e^-_{CB\,(ZnO)} \rightarrow Fe^{2+} \quad (5)$$

$$Fe^{2+} + O_2 \rightarrow Fe^{3+} + O_2^- \quad (6)$$

$$Fe^{2+} + S_2O_8^{2-} \rightarrow Fe^{3+} + SO_4^{2-} + SO_4^{\bullet-} \quad (7)$$

$$Fe^{3+} + S_2O_8^{2-} \rightarrow 2SO_4^{\bullet-} + Fe^{2+} \quad (8)$$

$$SO_4^{\bullet-} + H_2O \rightarrow SO_4^{2-} + OH^{\bullet} + H^+ \quad (9)$$

The enhancement of degradation by addition of Fe^{3+} ion was due to the electron scavenger effect of Fe^{3+}, which prevented an e^--h^+ recombination, resulting in an increase of the efficiency of photodegradation process [17,19].

Kinetic photocatalytic degradation of 2,4-DCP based on initial rate method was studied. Different initial concentrations of 2,4-DCP were tested. The degradation profiles are shown in Fig. 10(b). It was found that 2,4-DCP was degraded by 100, 77.6, 63.3, 60.3, and 46.3% within 90 min when initial concentration was applied at 5.0, 7.5, 10.0, 12.5, and 15.0 mg L^{-1}, respectively.

We applied the three point numerical differentiation formula to find the initial degradation rate (r_0) for each initial concentration (C_0). Since the degradation involves surface adsorption simultaneously with reaction, a Langmuir-Hinshelwood (L-H) rate expression was used to express its apparent kinetics [33,35,36]. The linear form of L-H is expressed in Eq. (10).

$$\frac{1}{r_0} = \frac{1}{k_r K_{ad} C_0} + \frac{1}{k_r} \quad (10)$$

where k_r is reaction rate constant (mg L^{-1} min^{-1}), K_{ad} is the adsorption equilibrium constant (L mg^{-1}), and C_0 is initial concentration of 2,4-DCP (mg L^{-1}).

As shown in Fig. 11 the linearity of this plot was used to determine the adsorption constant (K_{ad}) and reaction rate constant (k_r). They were equal to 0.089 L mg^{-1}, and 0.559 mg L^{-1} min^{-1}, respectively. Consequently, an apparent rate constant (k_{app}) was equal to 0.050 min^{-1}. The results demonstrated that the kinetics of 2,4-DCP photocatalytic degradation under our experimental conditions followed well the L-H rate equation (R^2=0.990).

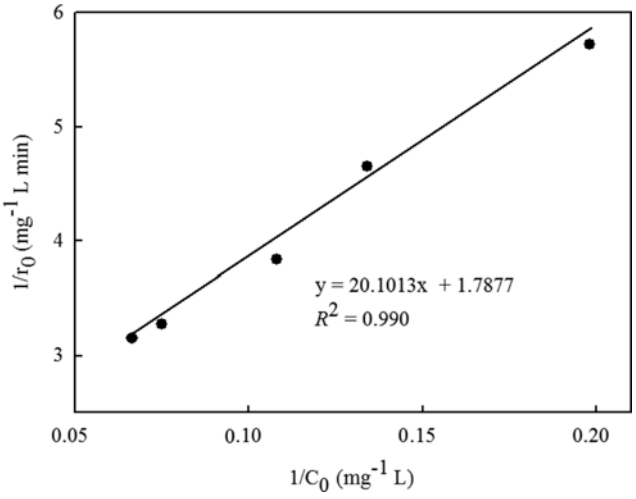

Fig. 11. Linearized Langmuir-Hinshelwood plot between $1/r_0$ and $1/C_0$.

CONCLUSIONS

Fe content (0.5, 2.5, and 5.0 mol%) and calcination temperature (400, 550, and 700 °C) were highlighted on Fe-ZnO synthesis via impregnation technique. UV-DRS results presented that visible light absorption of Fe-ZnO samples increased with increasing of Fe content and calcination temperature. Fe species (FeO, Fe_3O_4, and Fe_2O_3) on ZnO nanopowder as a function of calcinations temperature were found from TEM images. XANES analysis confirmed the majority of Fe^{3+} on ZnO nanopowder. Through RSM, under controlled parameters of 25 °C, 5.0 mg L^{-1} of 2,4-DCP, pH 8.5, and 2 mM $K_2S_2O_8$ as an oxidant, the best condition was observed at Fe loading of 4.5-5.0 mol%, calcination temperature of 680-700 °C, and catalyst loading of 1.2-1.8 g L^{-1}. The kinetic study of 2,4-DCP photodegradation was described by the Langmuir-Hinshelwood model (R^2=0.990). The apparent rate constant (k_{app}) was 0.050 min^{-1}.

ACKNOWLEDGEMENT

The authors would like to thank HSM, Chulalongkorn University and National Research Council of Thailand for the financial support and Synchrotron Light Research Institute (Nakhon Ratchasima, Thailand) for XAS measurement.

REFERENCES

1. J. F. Zhang, H. Liu, Y. Y. Sun, X. R. Wang, J. C. Wu and Y. Q. Xue, *Environ. Toxicol. Phar.*, **19**, 185 (2005).
2. Y. Li, X. Li and Y. Q. Li, *Environ. Pollut.*, **157**, 1879 (2009).
3. K. M. Ponvel, D. Kavitha, K. M. Kim and C. H. Lee, *Korean J. Chem. Eng.*, **26**, 1379 (2009).
4. A. A. Khodja, T. Sehili, J. F. Pihichowski and P. Boule, *J. Photoch. Photobio. A.*, **141**, 231 (2001).
5. D. Li and H. Haneda, *Chemosphere*, **51**, 129 (2003).
6. R. Wang, J. H. Xin, Y. Yang, H. Liu, L. Xu and J. Hu, *Appl. Surf. Sci.*, **227**, 312 (2004).
7. M. S. Nahar, K. Hasegawa and S. Kagaya, *Chemosphere*, **65**, 1976 (2006).
8. C. Shifu, Z. Wei, Z. Sujuan and L. Wei, *Chem. Eng. J.*, **148**, 263 (2009).
9. X. Zhang and L. Lei, *Mater. Lett.*, **62**, 895 (2008).
10. M. A. Bezerra, R. E. Santelli, E. P. Oliveira, L. S. Villar and L. A. Escaleira, *Talanta*, **76**, 965 (2008).
11. P. K. Sharma, R. K. Dutta, A. C. Pandey, S. Layek and S. L. Verma, *J. Magn. Magn. Mater.*, **321**, 2587 (2009).
12. A. Bera and D. Basak, *ACS Appl. Mater. Interfaces*, **2**, 408 (2010).
13. X. Lü, N. Lü, J. Gao, X. Jin and C. Lü, *Polym. Int.*, **56**, 601 (2007).
14. M. W. Porambo, H. R. Howard and A. L. Marsh, *J. Phys. Chem. C*, **114**, 1580 (2010).
15. C. Chen, K. L. Teo, T. C. Chong, Y. H. Wu, T. Osipowicz and M. A. Rahman, *J. Cryst. Growth*, **264**, 58 (2004).
16. M. B. A. Abdul, A. H. Kadhum, A. B. Mohamad, M. S. Takriff, and K. Sopian, *Chemosphere,* **91**, 1604 (2013).
17. S. Yi, J. Cui, S. Li, L. Zhang, D. Wang and Y. Lin, *Appl. Surf. Sci.*, (2014), http://dx.doi.org/10.1016/j.apsusc.2014.06.151.
18. L. Han, D. Wang, Y. Lu, T. Jiang, L. Chen, T. Xie and Y. Lin, *Sensor. Actuat. B-Chem.,* **177**, 34 (2013).
19. Q. Yin, R. Qiao, L. Zhu, Z. Li, M. Li and W. Wu, *Mater. Lett.*, **135**, 135 (2014).
20. J. Z. Kong, A. D. Li, H. F. Zhai, Y. P. Gong, H. Li and D. Wu, *J. Solid State Chem.*, **182**, 2061 (2009).
21. C. Liu, D. Meng, H. Pang, X. Wu, J. Xie, X. Yu, L. Chen and X. Liu, *J. Magn. Magn. Mater.,* **324**, 3356 (2012).
22. S. Karamat, R. S. Rawat, P. Lee, T. L. Tan and R. V. Ramanujan, *Prog. Nat. Sci.: Mater. Int.*, **24**, 142 (2014).
23. S. Maensiri, P. Laokul and V. Promarak, *J. Cryst. Growth*, **289**, 102 (2006).
24. K. M. Choi, S. Augustine, Y. M. Kim, J. H. Lee, J. Y. Lee and J. K. Kang, *J. Mater. Chem.*, **21**, 15175 (2011).
25. T. Yoon, J. Kim, J. Kim and J. Lee, *Energies*, **6**, 4830 (2013).
26. P. Sun, C. Wang, X. Zhou, P. Chen, K. Shimanoe, G. Lu and N. Yamazoe, *Sensor. Actuat. B-Chem.,* **193**, 616 (2014).
27. Y. Hou, Z. Xu and S. Sun, *Angew. Chem. Int. Ed. Engl.*, **46**, 6329 (2007).
28. A. P. C. Teixeira, J. C. Tristão, M. H. Araujo, L. C. A. Oliveira, F. C. C. Moura, J. D. Ardisson, C. C. Amorim and R. M. Lago, *J. Braz. Chem. Soc.*, **23**, 1579 (2012).
29. X. X. Wei, C. Song, K. W. Geng, F. Zeng, B. He and F. Pan, *J. Phys.: Condens. Matter*, **18**, 7471 (2006).
30. Agency for Toxic Substances and Disease Registry, Toxicological Profile for Chlorophenols, U.S. Department of Health and Human Services, Atlanta, Georgia (1999).
31. H. L. Liu and Y. R. Chiou, *Chem. Eng. J.*, **112**, 173 (2005).
32. R. Saleh and N. F. Djaja, *Superlattices Microstruct.*, **74**, 217 (2014).
33. M. A. Behnajady, N. Modirshahla and R. Hamzavi, *J. Hazard. Mater.*, **133**, 226 (2006).
34. K. Naeem and F. Ouyang, *J. Environ. Sci.*, **21**, 527 (2009).
35. M. Lackhoff and R. Niessner, *Environ. Sci. Technol.*, **36**, 5342 (2002).
36. E. Evgenidou, K. Fytianos, and I. Poulios, *Appl. Catal. B-Environ.*, **59**, 81 (2005).